Device

Article

Photochemical iontronics with multitype ionic signal transmission at single pixel for self-driven color and tridimensional vision

Graphical abstract

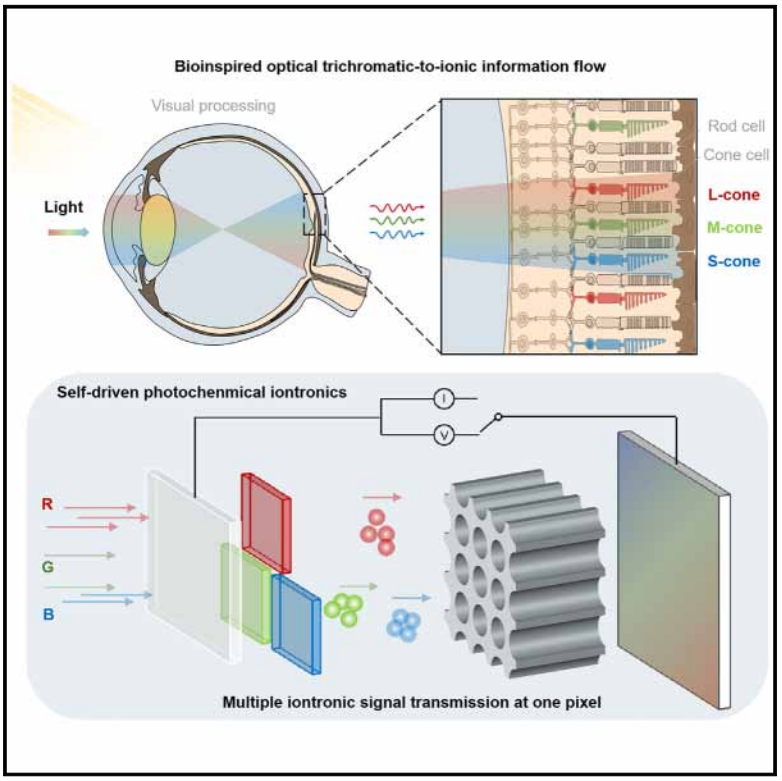

Highlights

- Photochemical iontronics can utilize multitype ions to process optical signals
- The device is self-driven and can exhibit cascaded high photovoltage up to 22 V cm^{-2}
- The vertical nanoconfined channels ensure the various independent ion transports
- Single-layer iontronic array can recognize trichromatic images for 3D reconstruction

Authors

Puguang Peng, Penghui Shen, Han Qian, ..., Tianling Ren, Zhonglin Wang, Di Wei

Correspondence

zhong.wang@mse.gatech.edu (Z.W.), dw344@cam.ac.uk (D.W.)

In brief

This study presents bioinspired photochemical iontronics that mimic the visual processing of the human eye. This device captures trichromatic light information and converts it into multiple ionic signals using different ions for each wavelength. This self-driven iontronic device integrates sensing, memory, and processing at a single pixel, offering a novel pathway for color recognition and potential applications in neuromorphic computing and human-machine hybrid intelligence systems.

1 Understand
Early stage research on device properties, design, and physics

Peng et al., 2025, Device 3, 100574
March 21, 2025
https://doi.org/10.1016/j.device.2024.100574

CellPress

Device

CellPress
OPEN ACCESS

Article

Photochemical iontronics with multitype ionic signal transmission at single pixel for self-driven color and tridimensional vision

Puguang Peng,[1,2] Penghui Shen,[3] Han Qian,[1,2] Jiajin Liu,[1,2] Hui Lu,[1,2] Yanyan Jiao,[4] Feiyao Yang,[1] Houfang Liu,[3] Tianling Ren,[3] Zhonglin Wang,[1,5,6,7,*] and Di Wei[1,8,9,*]

[1]Beijing Institute of Nanoenergy and Nanosystems, Chinese Academy of Sciences, Beijing 101400, China
[2]School of Nanoscience and Engineering, University of Chinese Academy of Sciences, Beijing 100049, China
[3]School of Integrated Circuits & Beijing National Research Center for Information Science and Technology, Tsinghua University, Beijing 10084, China
[4]Qitaihe Baotailong Graphene New Materials, Qitaihe, Heilongjiang 154600, China
[5]School of Materials Science and Engineering, Georgia Institute of Technology, Atlanta, GA 30332, USA
[6]Guangzhou Institute of Blue Energy, Knowledge City, Huangpu District, Guangzhou 510555, China
[7]Beijing Key Laboratory of Micro-Nano Energy and Sensor, Center for High-Entropy Energy and Systems, Beijing Institute of Nanoenergy and Nanosystems, Chinese Academy of Sciences, Beijing 101400, China
[8]Centre for Photonic Devices and Sensors, University of Cambridge, 9 JJ Thomson Avenue, CB3 0FA Cambridge, UK
[9]Lead contact
*Correspondence: zhong.wang@mse.gatech.edu (Z.W.), dw344@cam.ac.uk (D.W.)
https://doi.org/10.1016/j.device.2024.100574

THE BIGGER PICTURE One of the primary challenges in artificial intelligence hardware lies in optimizing information acquisition, processing, and energy consumption. Modern deep learning tasks increasingly depend on unstructured data such as text, images, and video, exposing the limitations of conventional von Neumann architectures. To overcome this bottleneck, there is a growing need for novel neuromorphic devices inspired by biological systems. Drawing from the process of biological vision, we have developed photochemical iontronics that utilize multitype ions as carriers of optical information, integrating sensing, processing, and memory within a single pixel. This system captures color information via light-triggered chemical reactions and modulates the transport of multitype ions through nanoconfined channels. The ion modulation mechanism presents a potential bridge for future human-machine hybrid intelligence. Furthermore, this self-driven, printable, and conformable device enables single-layer color recognition without complex artificial neural networks. When combined with a neural radiance fields algorithm, it can simulate and reconstruct high-fidelity, three-dimensional color images without the need for depth sensors.

SUMMARY

Most electronics and iontronics are high-throughput limited due to using electron or single-type ions for signal transmission. To store information within ions, a mechanism for transmission and processing of multitype ionic signals is needed to achieve integrated bio-functional iontronics. Here, we introduce photochemical iontronics that leverages controlled different ion transport in nanoconfined channels and meticulously designed photochemical redox reactions to send high-throughput iontronic signals. All iontronic signals can be distinguished by cascaded photovoltages consistent with the Nernst equation (up to $\sim$22 V cm^{-2}), providing tunable multiple non-volatile states for neuromorphic behaviors within the device based on light intensity and wavelength. Optical trichromatic-to-ionic information stored in a single-layer iontronic retinal array can be directly recognized without complex artificial neural networks, facilitating subsequent spatial 3D reconstruction. We expect that photochemical iontronics would be a potential candidate for future artificial intelligence applications based on ions.

INTRODUCTION

Recognizing environmental stimuli and controlling diverse iontronic signals to achieve precise bionic functions remain one of the primary challenges in the field of iontronics. State-of-the-art electronics and iontronics are still predominantly limited to electrons or single ions as charge or signal carriers, leaving the potential of ions as information storage units underexploited. Recent advancements in artificial electronic and iontronic systems have begun to bridge the information gap between nonbiological and biological interfaces, garnering considerable attention for their applications in bionic sensors,[1,2] iontronic prosthetics,[3,4] and implantable/conformable neuromorphic devices.[5,6] Among these, visual perception, a principal means by which organisms acquire environmental information, is considered crucial to the future of brain-machine hybrid intelligence.[7,8] By directly utilizing programmable photocurrent signals, it is possible to mimic the perception, processing, and memory functions of the retina and human brain.[9–12] However, unlike biological vision-to-neuron networks, which convey visual neural action potentials through diverse optical-to-ionic signal transduction (Figure 1A), most bionic eyes are constrained by their reliance on single-type electronic or ionic signal carriers. This limitation hampers their ability to carry and store richer biocompatible information, such as color and spatial data. Conventional switch-type bionic eyes, constructed from silicon-based,[13] perovskite,[8] and gel heterostructures,[10] struggle to differentiate between various ions and fail to faithfully replicate the high-throughput multitype ion co-transport characteristics of biological retinas. This inadequacy restricts their potential expression in matched biological retinal feature signals. Achieving light-stimulated multitype ion transport and processing to real visual applications remains a formidable challenge both in bionic eyes and iontronics.

In addition, integrating all desired biological functionalities simultaneously presents considerable challenges, including parallel high-throughput signal processing at one-pixel, synaptic responses, self-driven capabilities, bipolar color and spatial recognition, and conformal biocompatibility, as depicted in the radar map in Figure 1B. Current bionic eyes often exhibit limited high-throughput performance, primarily due to their output of single-type electronic or ionic current signals at an individual pixel, as discussed above. Furthermore, bionic eyes must demonstrate exceptionally low power consumption and, ideally, self-driven operation, yet the majority of currently available devices requires bias to function. Recent developments have shown that some bionic eyes exhibit negligible photovoltage (<0.1 V) and minimal photocurrents at 0 V bias (<1 μA) at each pixel, which hinders practical self-driven applications.[10,14–16] Enhancing the self-driven capability of these devices relies on amplifying the zero-voltage photocurrent and photovoltage, which directly correlates with improved optical recognition resolution. The challenge stems from the reliance of most devices on physical photoelectric or photothermal effects to trigger small built-in electric fields or electrical double layers (EDLs).[9,10,14,16] These effects are often insufficient to drive directed electron/ion migration effectively. Moreover, bionic retinal arrays must achieve wide-field detection for accurate three-dimensional (3D) reconstruction of the real-world objects, necessitating conformal preparation to accommodate diverse surface complexities.[17,18] While recent advancements frequently depend on costly materials or intricate techniques like microneedle positioning and lithography to impart curvature, flexibility, stretchability, and elasticity to bionic eyes, they present challenges for large-scale and cost-effective manufacturing processes.[8,11,13,19] Last but not least, color vision is a fundamental aspect of human eyes and holds significant importance for future human-machine hybrid vision. However, the realization of a practical self-driven bionic eye for color vision remains elusive, as previous attempts have yielded insufficient color resolution when applied at 0 V bias in practical self-driven scenarios, utilizing perovskite nanowires.[14,15]

Bioinspired iontronics holds promise for addressing current challenges in bionic eyes. All biological systems operate on principles akin to nanoconfined iontronics, in which ions as charge carriers could be effectively regulated due to the anomalous ionic dynamics within the nanoconfined structures.[20] Ions themselves also carry information and have specific functions in biological systems.[21,22] Both neurotransmission information transfer and ATP energy-conversion processes rely on precise ion transport through protein nanopores.[23,24] With its fundamental units of synapses and neurons, the human brain excels in multitasking and processing complex computations at exceedingly low power consumption (∼20 W).[20,25] The core scientific techniques of iontronics focus on emulating bionic control over ion dynamics and optimizing the ionic-electronic coupling interface, leading to the development of diverse iontronic sensors and power sources.[20,26,27] Similar to natural ion channels, ion dynamics within nanoconfined artificial channels with diameters under 100 nm are significantly enhanced by electrostatic forces.[28] Recent studies have shown that coupling interfaces such as EDLs or chemical reactions can further boost nanoconfined ion dynamics.[29–31] Cascade voltages, consistent with the Nernst equation, can be observed due to the different reactions at the ionic-electronic interface. Light-triggered iontronics, encompassing ion pumps, switches, and photochemical active centers, typically utilize physical photovoltage effects or organic molecule photochemical isomerization reactions to harvest and convert light energy, albeit with limited applications in optical information capture.[32–34] Exploring light-triggered diverse ion dynamics at the ionic-electronic interface unleashes the full potential of ions as charge and information storage units, enabling effective optical multitype iontronic signaling.

In this work, we present the fabrication of self-driven photochemical iontronics (PCI) through low-cost conformal printing, enabling multitype iontronic information transmission based on different ions at a single pixel, mirroring biological visual and brain functions. By coupling the light-triggered silver halide (AgX, where X = Cl^-, Br^-, and I^-) redox reactions with anionic transport in positively charged nanoconfined channels of nanoporous anodized aluminum oxide (AAO), specific photovoltages of about 0.88, 0.7, and 0.3 V can be detected at one pixel; these are consistent with the ion dynamics of Br^-, Cl^-, and I^- from the light-triggered redox reactions and Nernst equation expectations. The vertical nanoconfined channels and fast ion transport dynamics in AAO guarantee ion transport

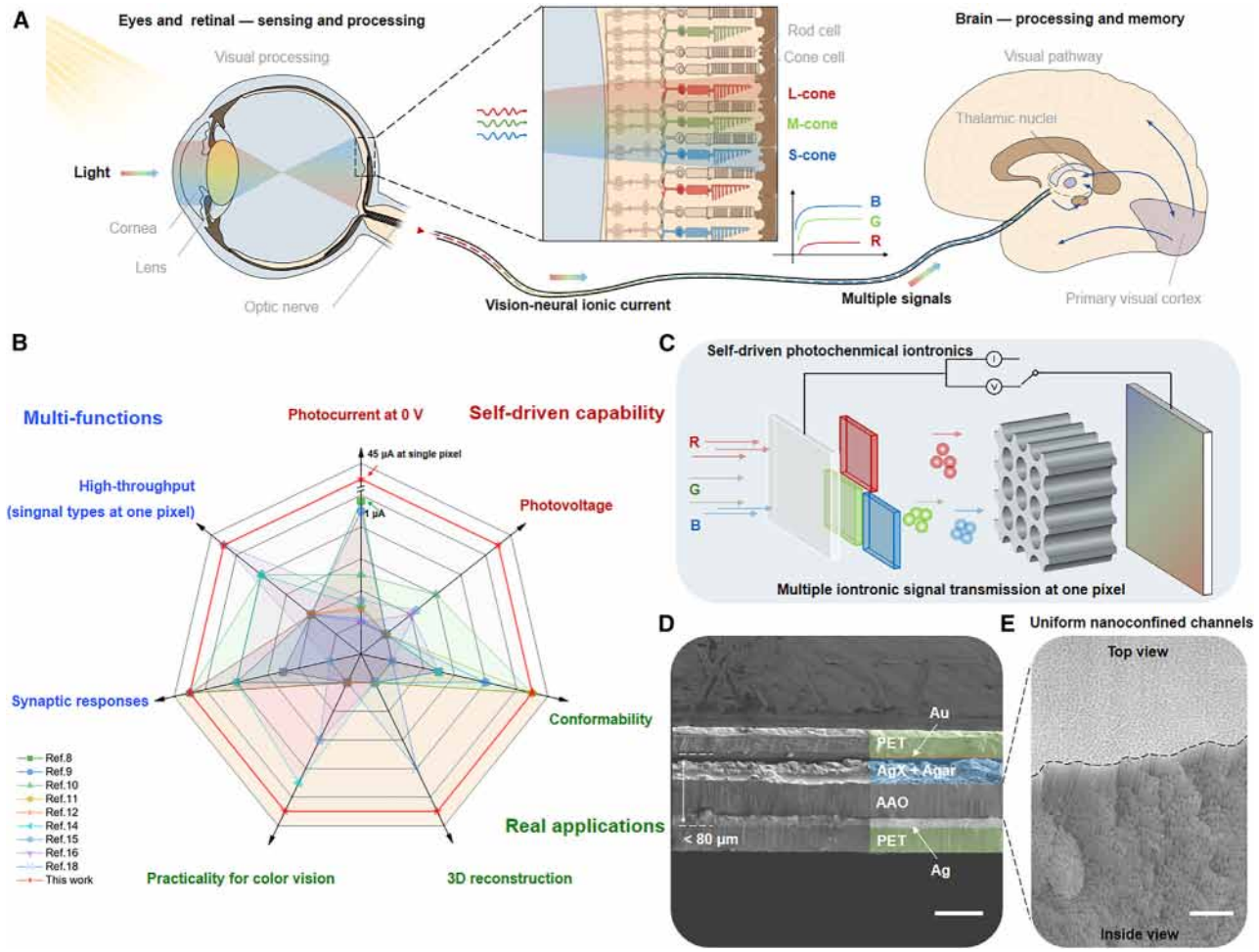

Figure 1. The design and functionality of the PCI

(A) Biological visual process and pathway. Detail of the structure of the human eye and its connection to the brain. Light enters the eye through the cornea and lens, and the optic nerve transmits the processed visual information as vision-neural ionic currents. The inset highlights the rod cells and cone cells (L-cone, M-cone, S-cone) responsible for detecting different wavelengths of light (RGB), which generate multiple signals transmitted to the brain for visual processing and memory.

(B) Schematics of the radar chart that compares the performance metrics of the PCI with various recent references. The pale-yellow area shows the comparison of qualitative metrics. "Synaptic responses" refers to the device's ability to integrate sensing, memorizing, and processing functions. "Practicality for color vision" indicates the device's ability to recognize colors. "3D reconstruction" refers to the device's ability to perform 3D image reconstruction, and "Conformability" represents the device's flexibility. All qualitative comparisons in the panel are made based on the degree of functionality for each feature.

(C) Schematics of the PCI, which shows multiple iontronic signal transmissions simultaneously at one pixel, carrying different optical information (RGB).

(D) SEM of the cross-sectional PCI; scale bar, 50 μm.

(E) Magnified SEM image of the AAO uniform nanoconfined channels from the top and inside views; scale bar, 500 nm. These channels are essential for the controlled transport of ions, contributing to the device's high-throughput and multifunctional capabilities.

independence for each anionic type. To establish correspondences between ions and optical color information, AgX is dyed, enabling the definition of these specific photovoltage signals as RGB (red, green, blue) parameters for trichromatic recognition and memory. With the inherent light-triggered redox reactions, the PCI can operate without external bias and exhibit unprecedented cascaded high photovoltage (up to ~22 V cm^{-2}) and ionic photocurrent multitype signals (up to ~1,125 μA cm^{-2}). All iontronic signals could provide multiple non-volatile states for neuromorphic processing in a device. The non-volatile photovoltage and photocurrent, carrying ion information, can be adjusted by light intensity and wavelength, indicating various neuromorphic behaviors such as perceiving, processing, and memorizing various pieces of visual information. In addition, the conformal printing can allow the PCI to be fabricated in non-planar surfaces, especially biomorphic curved and flexible structures. This functional integration has surpassed most currently reported bionic eyes, which renders it particularly suitable for simulating the functions of visual cone cells. As a demonstration, we have designed a single-layer iontronic retinal array for self-driven trichromatic recognition without resorting to complex artificial neural networks. In addition, this device can

be leveraged to simulate and reconstruct high-fidelity color real-world images using neural radiance fields (NeRF) without any depth sensor.

RESULTS AND DISCUSSION

Bioinspired design and structure of PCI

In the biological visual system, light can be captured by photoreceptors on the retina, such as cone and rod cells, leading to the generation of diverse action potentials that are ultimately transmitted through the axons of the optic nerve to the visual cortex in the brain, thereby forming vision[35] (Figure 1A). Among these photoreceptors, different types of cones (short-wavelength, medium-wavelength, and long-wavelength cones) contain various visual pigment molecules that are sensitive to different wavelengths of light. Upon exposure to light of different colors, the photoreceptors activate specific ion channels on the cell membrane through biochemical reactions, generating distinctive action potentials, which form the basis of bipolar color recognition[36,37] (Figures S1A and S1B). Moreover, all the energy involved in the biological visual process is derived solely from biochemical reactions, such as ATP hydrolysis (Figure S1C), without the need for external bias, hence requiring ultra-low power consumption of picowatts per individual cone cell.[38] Inspired by this process, we propose self-driven PCI with multitype ionic signal transmission at a single pixel, as illustrated in Figure 1C, which integrated functionalities, including bipolar trichromatic recognition, high-throughput multitype iontronic signals processing, and non-volatile memory. Additionally, given that the retina comprises ~6 million cone cells and exhibits a flexible hemispherical shape, the iontronics can be conformal-printed onto any elastic, flexible, and curved substrate via conformal printing.

The specific structure of individual PCI, as shown in Figures 1C and 1D, features a thickness under 80 μm and employs a simple and customizable manufacture for scalability, as illustrated in Figure S2. To mimic the photochemical sensitivity of different colors in cones, the photosensitive layer comprises three nanoporous agar AgX emulsions capable of distinguishing colors, as shown in Figure S3. AgX, as a stable photosensitive material, is used as the light-trigged ion source and is easily prepared in conjunction with agar through liquid-phase precipitation methods. The selection of nanoporous agar is attributed to its flexibility, biocompatibility, and high transparency, allowing the rapid movement of halide ions within the interstitial gaps, making the PCI more adaptable to the biological ion regulation and harboring potential for human-machine interface applications. After staining with trichromatic dyes, the emulsions permit the passage of color light with peak wavelengths of 581.6, 523.8, and 428.8 nm, respectively, aligning with the photochemical responses in human cone cells (Figure S4). The prepared photosensitive emulsions also possess excellent rheological properties suitable for conformal printing onto transparent Au-coated polyethylene terephthalate (PET) films to form photosensitive working electrodes, with adjustable printing thicknesses, reaching a minimum thickness of ~1 μm (Figures S5 and S6). It is noteworthy that due to the complex fabrication of traditional photodetectors, such as photolithography,[17] gas-liquid phase deposition,[14] and metal microneedle processes,[8] it is challenging to efficiently and cost-effectively achieve small single-pixel sizes on curved surfaces. Through nanoimprinting, the average spacing of PCI is expected to be reduced to the microscale, achieving the same pixel density as photosensitive cells in the human retina (10^7 cm^{-2}; Figure S7). To simulate the synaptic activity of peak neural ionic current transport from axons to the visual cortex in the brain, uniform nanoporous AAO membranes serve as positively charged nanoconfined channels for selecting halide ions, as shown in Figure 1E, interfacing with screen-printed Ag counter electrodes. The surface charge of AAO was modified positively by H^+ because protonation of the inner walls of AAO channels can occur[39] when the pH is below 10, with maximum positivity at pH = 3 (Figure S8). The nanoporous AAO has good light transmittance, with uniformly vertical nanoscale channel diameters of ~50 nm, as shown in Figure S9. When the nanochannel diameter is less than 100 nm, electrostatic attraction on the inner walls of the channels causes an abnormal enhancement of ion dynamics in the nanoconfined space.[20] We also conducted ion dynamics validation of nanoporous AAO channels with different alkali chlorides, as shown in Figure S10, achieving an anion selectivity of 94.4% for AAO under a 1,000-fold anion gradient and demonstrating a high ion rectification ratio of I^+/I^- = 276, which facilitates diverse ionic neuronal signal transmission. The rapid ion dynamics and vertical channel structure of AAO enable it to suppress ion signal interference between trichromatic channels, processing different iontronic signals in parallel. Furthermore, room temperature ionic liquids (RTILs) are used to fill the agar and AAO nanocavities between the two electrodes, serving as a medium for directed ion diffusion. By selecting the appropriate metal wire, each PCI can be addressed and measured, akin to the human retina operation, where photoreceptor cells are connected to ganglion cells via optic nerve fibers.

Programmable PCI signals

Owing to its unique mechanism of light-triggered redox reactions coupled with diverse ion transport within nanoconfined channels, the PCI signals can be used to distinguish and encode optical information. In addition, the chemical built-in electric field makes all photochemical responses and high-throughput iontronic signals able to be tested under no external bias. UV pulses (365 nm, 35 mW cm^{-2}) were first employed to evaluate the photoresponses of each monochromatic PCI called AgBr-PCI, AgCl-PCI, and AgI-PCI, with an active printing area of 2 × 2 mm per iontronic pixel. Unlike conventional photoelectric detectors, the built-in photochemical redox reactions in iontronics enable them to simultaneously output unprecedented multitype iontronic signals and show synaptic responses. The photovoltage responses, as seen in Figure 2A, exhibit distinct reproducible plateaus for three iontronics upon light pulses. Significant photovoltage increases were observed for AgBr-PCI, AgCl-PCI, and AgI-PCI, with observed values of $V_{AgBr\text{-}PCI}$ = ~0.88 V, $V_{AgCl\text{-}PCI}$ = ~0.55 V, and $V_{AgI\text{-}PCI}$ = ~0.3 V, respectively, consistent with the expectations of the Nernst equation as discussed in Note S1. Notably, the maximum photovoltage density can reach 22 V cm^{-2} for AgBr-PCI, which is the highest photovoltage density that is practically applicable in current solar cells based

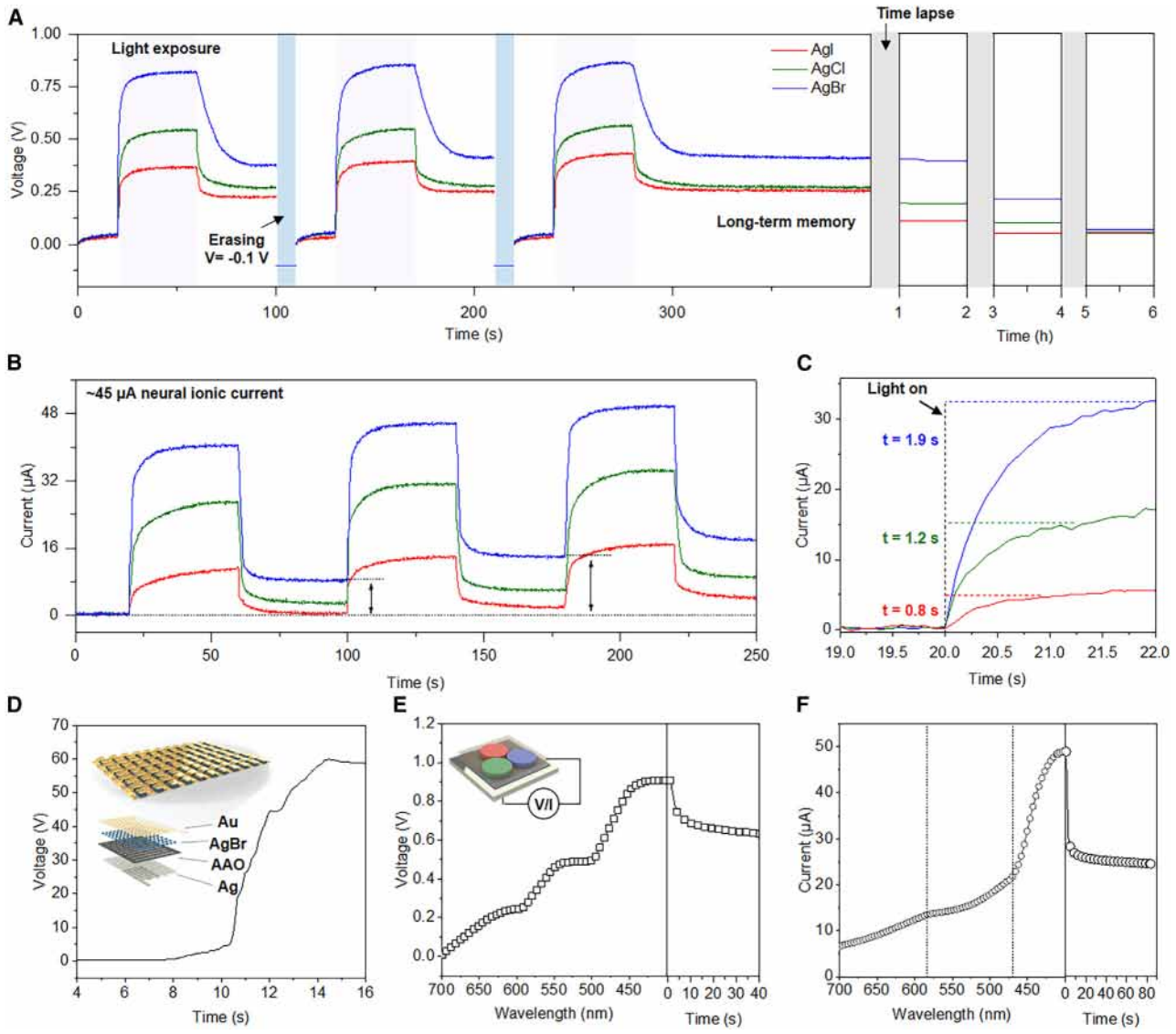

Figure 2. Photochemical synaptic responses with high-throughput iontronic signals

(A) Characteristic photovoltages of each iontronic with light writing (purple region) and voltage erasing (blue regions), showing an LTM that needs a long time to decay to the original level.

(B) Characteristic photocurrents of each iontronic.

(C) Response time of each iontronic, which is estimated based on the photocurrent approaching a steady state.

(D) High-throughput iontronic photovoltage signal at a printed PCI array with 110 AgBr-PCI (inset diagram).

(E) Light wavelength-modulated photovoltage responses in a trichromatic PCI. The dotted lines represent the photovoltage generated under different light wavelengths, ranging from 700 to 400 nm. These lines illustrate distinct voltage platforms corresponding to the specific photochemical reactions triggered by each sectional wavelength. These platforms allow for the identification of RGB colors based on the voltage output. The inset shows a schematic of the device with an RGB configuration for wavelength differentiation.

(F) Light wavelength-modulated photocurrent responses in the same trichromatic PCI. The dotted lines illustrate the photocurrent generated as a piecewise linear function of the light wavelength. Within each segmented range, the photocurrent increases linearly with the wavelength.

on Si,[40] organic,[41,42] and perovskite photovoltaic[43] as shown in Table S1. However, the photovoltage of AgI-PCI did not reach the Nernst expectation, which may be due to the weaker photosensitivity of AgI and poor ion transport dynamics in nanoconfined AAO channels resulting from the larger I^- hydrated radius as shown in Figure S11. After lights off, the photovoltage plateaus of each iontronic could be maintained stably for an extended period, reflecting an efficient learning capability akin to the human brain, acquiring long-term memory (LTM) with less stimulation. The difference in steady-state electrical signals before and after illumination was defined as the non-volatile memory signals. This non-volatile photovoltage could be erased

over time or through reverse electrical pulses (−0.1 V; blue region in Figure 2A), demonstrating the controllable photoetching and electrical erasure capabilities of the iontronics. The photocurrent responses, as shown in Figure 2B, reveal positive correlations to photovoltage transitions, with the AgBr-PCI exhibiting the largest light-responsive ionic photocurrent of ∼45 μA, followed by those from AgCl-PCI and AgI-PCI, with ionic photocurrents of ∼25 and ∼10 μA, respectively. In iontronic devices, the ionic current is strongly correlated with the ion dynamics at the bulk-electrode interface.[26,29,31] Here, the determining step of the photocurrent may be the interfacial light-triggered redox dynamics at the photosensitive working electrode, as Br^- with larger ionic radii and lower bulk diffusion coefficient (as shown in Table S2) obtained stronger ionic photocurrents than Cl^-. In detail, the intrinsic photochemical field provided by the light-triggered redox reaction at the AgBr interface exhibits the largest electromotive force (∼0.88 V) to drive ions, promoting unimpeded rapid anion transport in AAO channels. It is worth noting that the photocurrent density obtained from AgBr-PCI, ∼1,125 μA cm^{-2}, far exceeds the ionic photocurrents reported previously from photosystem centers,[44] photoelectric diodes,[9] photovoltaic ion pumps,[32] and photochromic switches,[34] as shown in Table S3, enabling our iontronics to better serve the ionic modulation of biology. After lights off, the photocurrents for each iontronics gradually decreased, likely due to the afterglow effect,[45,46] where the photochemical reactions did not immediately cease upon removing the illumination. Similar to biological systems, ion-based modulation systems lag behind artificial electronic systems in response speed, with light-triggered response times of the three devices being 1.9, 1.2, and 0.8 s, as shown in Figure 2C, respectively. However, this response relaxation time is a prerequisite for subsequent in-device perceiving and processing and is expected to enable the precise all-in-one strategies. Furthermore, white light pulses were also used to separately evaluate the photochemical responses of each iontronic, as shown in Figure S12. Under white light irradiation of 145 mW cm^{-2}, each PCI can still reach the same photovoltage plateau, but the response time increased. The distinctly differentiated photovoltage responses of the three iontronics will be defined as pseudo-trichromatic colors and can be used for subsequent color recognition related to light wavelengths. Figure S13 also showed that the volatile and non-volatile photocurrents of each PCI increase with the number of light pulses, eventually reaching similar outputs under UV light, which indicates that the electrical conductivity state of the iontronics can be continuously adjusted. This reflects short-term/long-term learning and memorizing capabilities that are similar to the human brain. To further demonstrate its high-throughput iontronic signals and scalability by conformal printing, we printed 110 PCI on 0.0005 m^2 that can achieve ∼55.7 V ultra-high photovoltage output, as shown in Figures 2D and S14, and S15. The unique photochemical response capability of iontronics to simultaneously output voltage and current signals lays the foundation for their subsequent use in self-driven applications.

To validate the ability to resist interference and multitype ionic signal transmission between the defined trichromatic channels, three photosensitive emulsions were printed on a single pixel to form a trichromatic PCI (T-PCI), and their light-response characteristics were tested using regulated light with continuously changing wavelengths. A schematic diagram of the test on a single pixel is illustrated in the Figure 2E inset. Based on the absorption curves of the trichromatic dyes (Figure S4), the photovoltage responses of the dyed iontronics exhibited discrete spectral response characteristics. As shown in Figure 2E, the photovoltage increased stepwise with the change in light wavelength, corresponding to the Nernst characteristic voltage of the three photosensitive emulsions, and gradually diminished upon light removal. This indicates that the transport of Cl^-, Br^-, and I^- between the trichromatic channels operates independently and processes various iontronic signals in parallel at the Ag electrode after responding to the light-triggered redox reactions. As trichromatic colors used by the human visual system to generate all other colors, the stepwise photovoltage responses enable PCI to precisely achieve trichromatic recognition. Furthermore, the T-PCI synaptic photocurrent response also exhibited staged linear responses within three different threshold wavelength ranges of 700–580, 580–475, and 475–400 nm, indicating that the input light can be used to obtain linear multilevel conductive states within different wavelength ranges and can better simulate the electrical activity of biological vision-neurons as shown in Figures 2F and S16. Even at low incident light power (11.6 mW cm^{-2}), the T-PCI could generate stable ionic photocurrents and demonstrate learning capabilities similar to those of the human brain (Figure S17). Additionally, the uniformity and stability of T-PCI performance were investigated in Figure S18, where the T-PCI could cycle stably for 10 h under light pulses at 0.1 Hz, and the photocurrent output could also be maintained under continuous light exposure.

Mechanism of PCI

The mechanism of the PCI is illustrated in Figure 3A. In our design, AgX was used as an ion source, and the photosensitive process primarily involves the light-triggered AgX redox reactions and the rapid transport of halide anions in the AAO nanoconfined channels. After illumination, photon energy is absorbed by the surface portion of the AgX crystals, forming photosensitive centers and causing electrons in the crystal to transition from the valence band (VB) to the conduction band (CB).[45,47] This transition generates a photoelectron (negative charge) to the CB, while leaving a photogenerated hole (positive charge) in the VB. The photoelectron/hole pair could participate in the electron transfer and lead to photochemical reactions. To obtain the band-gap structures of AgX, UV-visible (UV-vis) diffuse reflectance spectra and X-ray photoelectron spectroscopy (XPS) were used to test the band-gap energy (E_g) and VB energy level (E_{VB}) of AgX, thus predicting the CB energy level (E_{CB}), as shown in Figure S19. It is worth noting that for specific photochemical reactions to occur, the $E_{CB(VB)}$ of AgX needs to match its redox potential (relative to the normal hydrogen electrode),[48,49] as shown in Figure S20. Therefore, after illumination, the generated photoelectrons transfer to the surrounding AgX molecules, triggering the reduction of Ag^+ and releasing halide anions ($AgX + e^-_{hv} \rightarrow Ag + X^-$) in RTIL. The photogenerated holes, possessing strong oxidizing properties, can attract electrons and oxidize the Ag electrode directly ($Ag + X^- + h^+_{hv} \rightarrow AgX$) by conductor, creating a chemical built-in electric field.

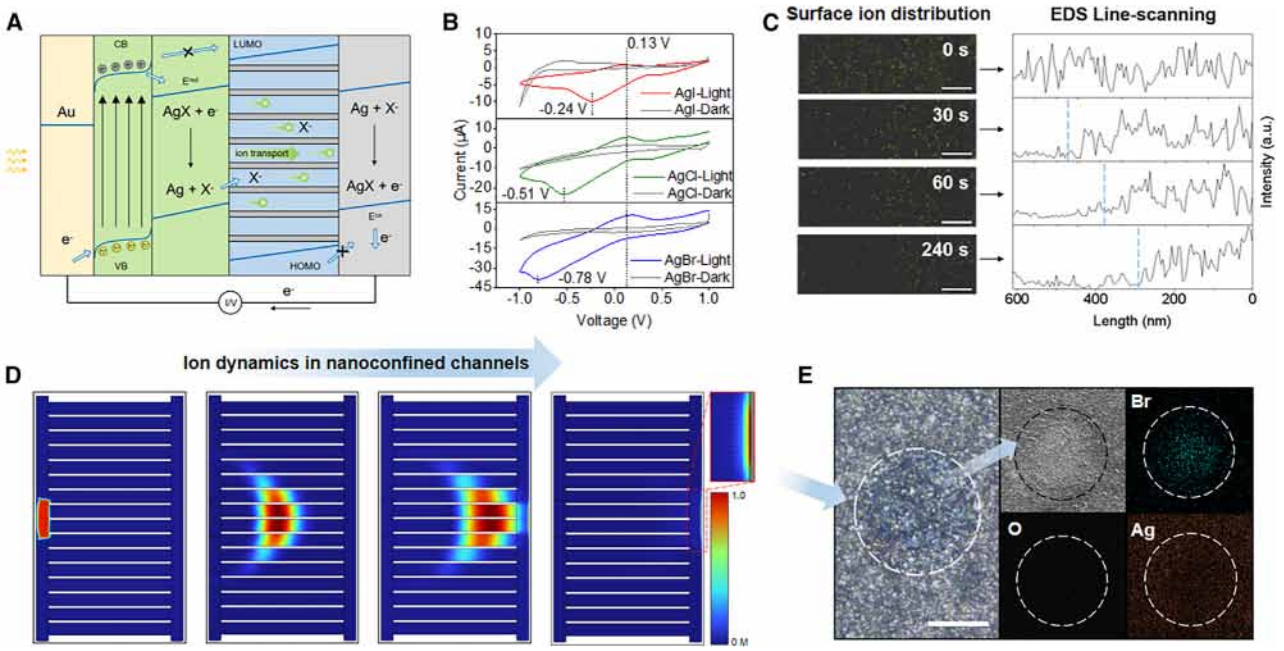

Figure 3. Mechanism and ion dynamics of the PCI

(A) Schematic illustrations of the mechanism of photochemical reactions coupling ion dynamics.

(B) Characteristic CV of each iontronic at 1 mV s^{-1}.

(C) Time-lapse EDS elemental mapping and linear scan curves of the surface ion distribution during exposure; scale bar, 100 nm.

(D) COMSOL simulation of the ion dynamics in AAO nanoconfined channels, depicting ion movement and concentration changes under light.

(E) The surface morphology and EDS elemental mapping of Br, O and Ag within the selected area; scale bar, 500 μm.

This built-in electric field, along with the ion gradient, drives the rapid transfer of the generated halide ions through the selective AAO nanoconfined channels. This feature was first observed by cyclic voltammetry (CV) testing, where distinct characteristic peaks corresponding to redox pairs of each AgX were obtained by all PCI after illumination, and the difference could be roughly estimated as the decomposition potential (Figure 3B). The photochemical potentials that consistent to the Nernst equation between the photosensitive working electrode and the Ag counter electrode would reflect the optical information carried by halide ions. Upon lights off, slow photovoltage/current decay due to the afterglow effects of light-trigged reactions and the uncoordinated ion transport rate in AAO would result in non-volatile storage of photovoltage/current. This photochemical mechanism differs from previous photovoltaic mechanisms and leads to unique integrated functions of self-driven in-device perceiving, processing, and memorizing. To verify this hypothesis, we selected the AgBr-PCI for exposure testing, as AgBr has the highest photochemical voltage. Experimental and simulation methods were used to describe the photochemical processes at the surface/interface, and the Br^- transport dynamics in the AAO nanoconfined channels during illumination. A continuous elemental analysis during exposure was performed with the selected region on the AgBr surface, as shown in Figures 3C and S21, where the energy-dispersive spectrometry (EDS) for elemental mapping spectrum and linear scan curves both indicated a gradual decrease in surficial Br, demonstrating the reduced reaction of AgBr and subsequent Br^- diffusion caused by the surface photochemical response. Surface XPS spectra also confirmed this phenomenon, showing a decrease in surface Br abundance after illumination, indicating a reduction in Ag-Br bonds (Figure S22). Furthermore, the light-driven ionic current was almost unobservable when there was no AgBr, indicating its indispensability (Figure S23). Subsequently, COMSOL simulation was used to simulate the transport of anions in the AAO nanoconfined channels; the configuration is shown in Figure S24. Video S1 also shows the dynamic ion transporting process. As shown in Figures 3D and Figure S25, after illumination, Br^- would be locally generated and constitute an asymmetric ion gradient for rapidly transporting through the anion selectivity AAO nanoconfined channels under the driven force of the redox chemical built-in electric field, eventually contacting the Ag counter electrode to form a hemispherical protrusion of oxide reaction centers. It is worth noting that the simulated results also showed that anion transport occurred within only a few nanoconfined channels, indicating that vertical AAO channels could suppress signal interference from different ions and process high-throughput iontronic signals in parallel. Linear voltammetry scans and electrochemical impedance spectroscopy of the PCI after illumination also showed significant enhancements in current and voltage due to the photo-ionic flow leaded resistance reducing (Figure S26), further confirming the rapid transport of ions in the AAO nanoconfined channels. Additionally, we verified the performance of the PCI using tetrabutylammonium bromide (TBABr) mixed with poly(vinylidene fluoride-co-hexafluoropropylene) (PVDF-HFP) as an anion-selective gel

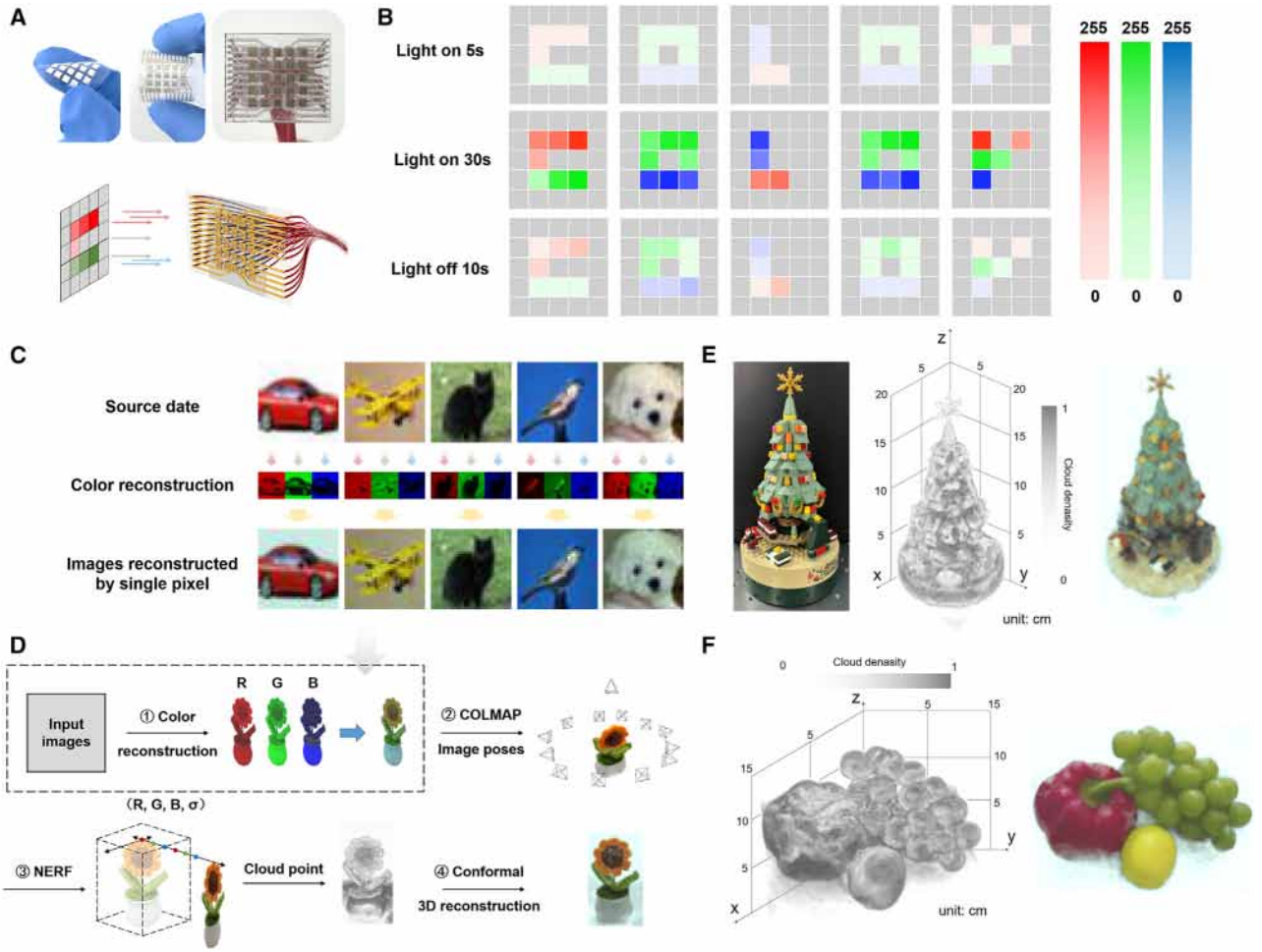

Figure 4. Optical trichromatic-to-ionic information flow for self-driven applications

(A) Photograph of our flexible, conformable iontronic retinal array and the illustration of the trichromatic recognition.

(B) The decoded image (trichromatic letter "color") of the iontronic retinal array with human eyes and brain functions.

(C) Samples of images from original and reconstructed dates by single iontronics.

(D) Architecture of the accurate 3D reconstruction that is decoded by artificial neural networks based on the color information carried by ions.

(E and F) Samples of the reconstructed spatial images from the original object.

instead of AAO, showing slower photoresponses and lower ionic photocurrents, possibly due to the lateral diffusion of ions in the gel leading to reduced ionic conductivity (Figure S27). Finally, the hemispherical protrusive oxide reaction centers on the Ag counter electrode surface were observed by optical microscopy and scanning electron microscopy (SEM)/EDS test (Figure 3E), revealing significant changes in surface morphology, and it was confirmed by X-ray diffraction (XRD) and EDS detection as the generation of AgBr (Figure S28). The distribution of Br^- ions on the Ag surface exhibited central diffusion, similar to the fitted results.

Optical trichromatic-to-ionic information flow for self-driven applications

The capability of PCI to recognize trichromatic light and output multitype ionic signals at a single pixel is akin to the cone cells and optic axons in human vision, enabling simultaneous perceiving, processing, and memorizing of optical information. Importantly, there has yet to emerge a truly self-driven iontronic retinal array that can use the ions to store the trichromatic information like creatures. Furthermore, employing a low-cost customized printing approach, these PCI can be fabricated conformally as curved retina arrays, which bodes well for future precise digital healthcare and virtual reality applications. All these features make PCI adept at mimicking the complex functions of the human eye, and its curved and ionic modulation also endows it with the potential to serve as a visual-human interface. As an illustration, we printed a 5 × 5 flexible T-PCI retinal array, which each iontronic can operate independently, as shown in Figures 4A and S29. Since PCI exhibit a stepwise photovoltage response to different ranges of light wavelengths (Figure 2E), it is possible to define the different photovoltages, which from the multitype ions transport, as trichromatic signals for color recognition. In addition, the produced interval photocurrents in

each range can be defined as the brightness information due to their linear change (Figures 2F and S16). This process will be implemented through a nested LabVIEW conditional control program in time sequences by converting it into octal values (Figure S30). Its optical trichromatic-to-ionic information flow and sensing function can be tested by directly projecting optical trichromatic letters onto the PCI array. Figure 4B shows the image of each trichromatic character "color" without the need for complex neural network setups. Within the first 5 s, trichromatic information identified by each pixel was accurately determined by photovoltage threshold, with the brightness enhanced in the subsequent 30 s by photocurrent information. Even after turning off the lights, trichromatic information can still be recorded, demonstrating the memory capacity of the PCI array. Video S2 showcases the dynamic process of sensing and processing trichromatic letters sequentially captured by the iontronic retinal array. Its unique mechanism of ions carrying information and synaptic behaviors enables it to extract RGB without additional bias, achieving high-fidelity trichromatic recognition.

In addition, the color information carried by ions can be decoded by artificial neural networks to obtain the spatial images. To further elucidate this applicable value, we conducted color reconstruction simulations of images based on single-pixel responses. For each image in Figure 4C, we simulated the images of the PCI based on the photocurrent values of each trichromatic channel collected in Figure S13. Then, the three photocurrents were normalized into three octal grayscale images and directly sent to the RGB channels to form the reconstructed image. Figure 4C illustrates examples of the original dataset and artificial retinal color reconstruction. Although the colors are slightly different from the original dataset, there is sufficient feature information for subsequent accurate 3D reconstruction. Traditional 3D reconstructions rely on expensive depth sensors, large equipment, and complex technologies such as computed tomography, MRI, ultrasound,[50] or laser positioning radar, making them difficult to generalize. Recent advances in neural network algorithms have demonstrated the ability to directly predict surface color and normal vector information of corresponding 3D scenes from inputting two-dimensional (2D) images with monocular characteristics, such as RGB, without the need for explicit 3D geometry parameters from depth sensors.[51,52] Figure 4D demonstrates our accurate 3D reconstruction model based on the algorithm of Colmap and NeRF. Given a set of artificial color reconstructed 2D images, Colmap first extracts and matches features to estimate their image poses. Based on these image poses and trichromatic information, NeRF can recover the positions of most pixels in the space, thus reconstructing the 3D scene. This model can effectively assist in reconstructing the real world with our low-cost conformable PCI. Figures 4E and 4F depict schematic diagrams of the accurate 3D reconstruction after color reconstruction, showcasing its potential applications in digital health care and virtual reality. Figure S31 also demonstrates that clear shapes can be reconstructed even under conditions of single-color, all-black, or all-white surfaces.

Conclusion

In summary, we have developed printable high-throughput, self-driven, and conformable PCI, inspired by biological vision. It enables multitype iontronic information transmission at a single pixel by leveraging light-triggered AgX redox reactions within nanoporous AAO nanoconfined channels. Such iontronics can achieve specific photovoltage signals (0.88 V for Br^-, 0.7 V for Cl^-, and 0.3 V for I^-) consistent with ion dynamics predicted by the Nernst equation. The vertical nanoconfined channels in AAO ensure independent ion transport for each anion type, facilitating accurate trichromatic recognition. Our PCI also operates without external bias, demonstrating exceptional cascaded high photovoltage ($\sim$22 V cm^{-2}) and ionic photocurrent multitype signals ($\sim$1,125 μA cm^{-2}), with the largest electromotive force compared to the previous self-driven bionic eyes. All iontronic signals, providing multiple non-volatile states, enable neuromorphic functionalities within the device, including perception, processing, and memorization of various pieces of optical information. Furthermore, the conformal printing technique allows fabrication on non-planar biomorphic curved and flexible surfaces, surpassing current bionic eye designs and making it suitable for simulating the functions of visual cone cells. To demonstrate, we have designed a single-layer iontronic retinal array capable of self-driven trichromatic recognition without complex artificial neural networks. This device also enables the simulation and reconstruction of high-fidelity color images of real-world scenes using NeRFs without depth sensors. These advancements pave the way for efficient retina transplantation and virtual reconstruction of real-world objects, accelerating the integration of digital health care and artificial intelligence applications in the future.

EXPERIMENTAL PROCEDURES

Conformal preparation of PCI and the array

To prepare the photosensitive layer, the transparent Au electrodes on PET were prepared by a magnetron sputtering film deposition system (Denton Discovery 635) at 20 mA for 120 s. We prepared 1 M potassium halides (KX, where X^- = Cl^-, Br^-, I^-) and 1 wt % agar mixed emulsions at 80°C and immediately printed on the transparent Au electrodes by a three-axis mechanical pneumatic liquid extrusion system from Fairchild Industrial Products Company to form the gel precursor. Afterward, 1 M $AgNO_3$ was used to precipitate the X^- ions in gel to form AgX and then immersed them in cold water (to avoid the agar dissolution) to remove K^+ and NO_3^- ions. To assign each PCI the ability to recognize tricolor, methyl red, methyl green, and methyl blue were used to dye the AgI-PCI, AgCl-PCI, and AgBr-PCI, respectively, and allow the corresponding color light to pass through. To prepare the AAO nanoconfined channels, the pure Al foil with a thickness of 50 μm was deformed and then cleaned by sonication in acetone and rinsed with isopropyl alcohol and water. The customized Al foil was electrochemically polished in an acidic solution (25 vol % $HClO_4$ mixed with 75 vol % absolute alcohol) for 10 min under 12 V at 10°C. After being polished and washed, the foil was anodized in 0°C, 0.3 M $H_2C_2O_4$ at 30 V, 100 mA for 10 h to obtain the AAO film. The AAO film was later floated on the H_3PO_4 solution (5 wt %, 60°C) for 10 min to open the channels. To form the ionic gel film to replace AAO and test the photochemical responses of the device, PVDF-HFP, purchased from Sigma-Aldrich, was dissolved by acetone and mixed uniformly with TBABr (10 wt %, 20 wt %, and 30 wt % vs. PVDF-HFP), and then dried at 80°C. To prepare the Ag electrode, Ag ink, purchased from Changsung, was screen-printed on the PET by using a predesigned screen-printing pattern. The RTILs were prepared by 0.01 M tetrabutylammonium halides (TBAX, where X^- = Cl, Br, I) in propylene carbonate. The photosensitive layer, AAO nanoconfined channels, and Ag electrodes were composed to form the PCI, as shown in Figures 1C and 1D. The PCI array (Figure S14) and the iontronic retinal array (Figure S29) were prepared by printing with the customized AAO and

electrodes. The conduct wires were used to connect each iontronic by through-hole technology. Hemispherical or conformal substrates can be prepared by deformation and printing as shown in Figures S2 and S7.

The target material Au (99.9999%) was purchased from ZhongNuo Advanced Material (Beijing) Technology. $AgNO_3$, KX, $HClO_4$, $H_2C_2O_4$, H_3PO_4, PVDF-HFP, TBAX, and propylene carbonate were purchased from Sigma-Aldrich and were used as received. Agar, methyl red, methyl green, and methyl blue were purchased from Aladdin. Ag ink (Paron-910 series) was purchased from ChangSung Corporation.

Characterization and measurements

Morphologies of the PCI were observed by the SEM (SU8020, Hitachi) with the 5.0 kV accelerating voltage, 10 μA emission current and the EDS was used for the element analysis. The micro-optical images of the devices were obtained using a metallographic microscope (UMT203i, Chongqing UOP). The structure of AAO was obtained by transmission electron microscopy (FEI Titan), with the operating voltage of 300 kV. Zeta potential was obtained by using a Beckman Coulter instrument (Delsamax Pro). The chemical states and band energy of the AgX were obtained using XPS (X-tool, PHI). XRD was carried out using a Bruker D8 ADVANCE system with a Cu Kα source. The Dektak XT stylus profiler (Brucker) was used to profile the morphology of the printed emulsions. The rheological property of the emulsions was measured with an Anton Paar MCR 301 rheometer under the parallel plate geometries, with a diameter of 25 mm and a gap of 0.5 mm. The infiltration ability of emulsions was characterized by a surface tension meter (Dataphysics OCA20). All electrochemical measurements were carried out with an electrochemical workstation (Multi Autolab M204). All linear voltammetry scans in liquid were tested by the standard Ag/AgCl electrodes unless otherwise noted. The electrochemical impedance spectrum was measured on an extended range from 1 MHz to 0.01 Hz. The photovoltage and photocurrent output were recorded by the Keithley electrometer 6514. A light-emitting diode driver (THORLABS, DC2200 Terminal) was used as the light source, and the optical incident power density was measured by an optical power meter (CEL-NP2000). UV-vis spectra were measured using an Agilent Cary 5000 UV-vis-near-infrared spectrophotometer. All measurements were carried out at RT.

Self-driven trichromatic recognition

A 5 × 5 iontronic retinal array was printed to perform the self-driven trichromatic recognition by using a home-built system consisting of a multiplexer (PXI-2530B, National Instruments), a voltage meter (TB-4300, National Instruments), a current meter (PXI-4130, National Instruments), a computer, and a Labview program without any bias. The schematic of the system can be found in Figure S29. The voltage and current meter, together with the multiplexer, were installed inside of a chassis (PXIe-1075, National Instruments). The LabVIEW schematic can be found in Figure S30. To realize the trichromatic recognition, trichromatic letters were generated by PowerPoint slides and projected directly onto the iontronic retinal array by a projector without a lens.

COMSOL calculations

The ion transport in AAO nanoconfined channels was systematically analyzed by a theoretical model based on Poisson-Nernst-Planck equations with proper boundary conditions,

$$\Delta^2\Phi = -\frac{F}{\varepsilon}\sum z_i c_i$$

$$j_1 = D_i \Delta c_i + \frac{z_i F}{RT} D_i c_i \Delta\Phi$$

$$\Delta \cdot j_i = 0,$$

where Φ, c_i, D_i, j_i, and z_i are the electrical potential, ion concentration, diffusion constant, ionic flux, and charge of species i, respectively. ϵ is the dielectric constant of the electrolyte solution. The boundary condition for potential Φ on the nanotube wall is

$$\vec{n} \cdot \nabla\Phi = -\frac{\sigma}{\varepsilon},$$

where σ is the surface charge density. The ion flux has the zero normal components at boundaries,

$$\vec{n} \cdot j = 0.$$

The geometric parameters are in Figure S24. For all the calculations, the accuracy is set to be less than 10^{-6}.

RESOURCE AVAILABILITY

Lead contact

Further information and requests for resources and reagents should be directed to and will be fulfilled by the lead contact, Di Wei (weidi@binn.cas.cn).

Materials availability

The materials generated in this study are available from the lead contact upon reasonable request.

Data and code availability

The data used to support the findings of this study are available from the lead contact upon reasonable request.

ACKNOWLEDGMENTS

We thank Shaoxin Li and Yan Du from the group of D.W. at the Beijing Institute of Nanoenergy and Nanosystems for their help with the mechanism and trichromatic recognition studies. This work was supported by the Beijing Natural Science Foundation (grant no. IS23040) and National Natural Science Foundation (grant no. 22479016).

AUTHOR CONTRIBUTIONS

D.W. and Z.W. proposed the idea and supervised the whole project. D.W. and P.P. designed the project and experiments. P.P., H.Q., and Y.J. carried out the fabrication and experiments of the materials and PCI. J.L. conducted the absorbance measurements and analyzed the data. P.P. and F.Y. fabricated the printed arrays and performed the circuits design and measurements. P.P. and H.L. prepared and performed the trichromatic recognition. P.P. and P.S. discussed and designed the algorithms for color and 3D reconstruction, and H.L. and T.R. provided some suggestions. All the authors discussed the results and commented on the manuscript. D.W. and P.P. wrote the paper.

DECLARATION OF INTERESTS

The authors declare no competing interests.

SUPPLEMENTAL INFORMATION

Supplemental information can be found online at https://doi.org/10.1016/j.device.2024.100574.

Received: July 23, 2024
Revised: September 5, 2024
Accepted: September 11, 2024
Published: October 11, 2024

REFERENCES

1. Xia, X., Spadaccini, C.M., and Greer, J.R. (2022). Responsive materials architected in space and time. Nat. Rev. Mater. *7*, 683–701. https://doi.org/10.1038/s41578-022-00450-z.
2. Zhao, S., Tseng, P., Grasman, J., Wang, Y., Li, W., Napier, B., Yavuz, B., Chen, Y., Howell, L., Rincon, J., et al. (2018). Programmable Hydrogel Ionic Circuits for Biologically Matched Electronic Interfaces. Adv. Mater. *30*, e1800598. https://doi.org/10.1002/adma.201800598.

3. Ortiz-Catalan, M., Zbinden, J., Millenaar, J., D'Accolti, D., Controzzi, M., Clemente, F., Cappello, L., Earley, E.J., Mastinu, E., Kolankowska, J., et al. (2023). A highly integrated bionic hand with neural control and feedback for use in daily life. Sci. Robot. *8*, eadf7360. https://doi.org/10.1126/scirobotics.adf7360.

4. Kweon, H., Kim, J.S., Kim, S., Kang, H., Kim, D.J., Choi, H., Roe, D.G., Choi, Y.J., Lee, S.G., Cho, J.H., and Kim, D.H. (2023). Ion trap and release dynamics enables nonintrusive tactile augmentation in monolithic sensory neuron. Sci. Adv. *9*, eadi3827. https://doi.org/10.1126/sciadv.adi3827.

5. Lee, Y., Liu, Y., Seo, D.-G., Oh, J.Y., Kim, Y., Li, J., Kang, J., Kim, J., Mun, J., Foudeh, A.M., et al. (2023). A low-power stretchable neuromorphic nerve with proprioceptive feedback. Nat. Biomed. Eng. *7*, 511–519. https://doi.org/10.1038/s41551-022-00918-x.

6. Chen, W., Zhai, L., Zhang, S., Zhao, Z., Hu, Y., Xiang, Y., Liu, H., Xu, Z., Jiang, L., and Wen, L. (2023). Cascade-heterogated biphasic gel iontronics for electronic-to-multi-ionic signal transmission. Science (New York, N.Y.) *382*, 559–565. https://doi.org/10.1126/science.adg0059.

7. Ersaro, N.T., Yalcin, C., and Muller, R. (2023). The future of brain–machine interfaces is optical. Nat. Electron. *6*, 96–98. https://doi.org/10.1038/s41928-023-00926-y.

8. Gu, L., Poddar, S., Lin, Y., Long, Z., Zhang, D., Zhang, Q., Shu, L., Qiu, X., Kam, M., Javey, A., and Fan, Z. (2020). A biomimetic eye with a hemispherical perovskite nanowire array retina. Nature *581*, 278–282. https://doi.org/10.1038/s41586-020-2285-x.

9. Chen, K., Hu, H., Song, I., Gobeze, H.B., Lee, W.-J., Abtahi, A., Schanze, K.S., and Mei, J. (2023). Organic optoelectronic synapse based on photon-modulated electrochemical doping. Nat. Photonics *17*, 629–637. https://doi.org/10.1038/s41566-023-01232-x.

10. Luo, X., Chen, C., He, Z., Wang, M., Pan, K., Dong, X., Li, Z., Liu, B., Zhang, Z., Wu, Y., et al. (2024). A bionic self-driven retinomorphic eye with ionogel photosynaptic retina. Nat. Commun. *15*, 3086. https://doi.org/10.1038/s41467-024-47374-6.

11. Wang, C., Bian, Y., Liu, K., Qin, M., Zhang, F., Zhu, M., Shi, W., Shao, M., Shang, S., Hong, J., et al. (2024). Strain-insensitive viscoelastic perovskite film for intrinsically stretchable neuromorphic vision-adaptive transistors. Nat. Commun. *15*, 3123. https://doi.org/10.1038/s41467-024-47532-w.

12. Huang, P.-Y., Jiang, B.-Y., Chen, H.-J., Xu, J.-Y., Wang, K., Zhu, C.-Y., Hu, X.-Y., Li, D., Zhen, L., Zhou, F.-C., et al. (2023). Neuro-inspired optical sensor array for high-accuracy static image recognition and dynamic trace extraction. Nat. Commun. *14*, 6736. https://doi.org/10.1038/s41467-023-42488-9.

13. Pang, X., Wang, Y., Zhu, Y., Zhang, Z., Xiang, D., Ge, X., Wu, H., Jiang, Y., Liu, Z., Liu, X., et al. (2024). Non-volatile rippled-assisted optoelectronic array for all-day motion detection and recognition. Nat. Commun. *15*, 1613. https://doi.org/10.1038/s41467-024-46050-z.

14. Long, Z., Qiu, X., Chan, C.L.J., Sun, Z., Yuan, Z., Poddar, S., Zhang, Y., Ding, Y., Gu, L., Zhou, Y., et al. (2023). A neuromorphic bionic eye with filter-free color vision using hemispherical perovskite nanowire array retina. Nat. Commun. *14*, 1972. https://doi.org/10.1038/s41467-023-37581-y.

15. Liu, Y., Ji, Z., Cen, G., Sun, H., Wang, H., Zhao, C., Wang, Z.L., and Mai, W. (2023). Perovskite-based color camera inspired by human visual cells. Light Sci. Appl. *12*, 43. https://doi.org/10.1038/s41377-023-01072-y.

16. Ding, Y., Liu, G., Long, Z., Zhou, Y., Qiu, X., Ren, B., Zhang, Q., Chi, C., Wan, Z., Huang, B., and Fan, Z. (2022). Uncooled self-powered hemispherical biomimetic pit organ for mid- to long-infrared imaging. Sci. Adv. *8*, eabq8432. https://doi.org/10.1126/sciadv.abq8432.

17. He, Z.-P., Han, X., Wu, W.-Q., Xu, Z.-S., and Pan, C.-F. (2024). Recent advances in bioinspired vision systems with curved imaging structures. Rare Met. *43*, 1407–1434. https://doi.org/10.1007/s12598-023-02573-w.

18. Chen, Y., Huang, Y., Zeng, J., Kang, Y., Tan, Y., Xie, X., Wei, B., Li, C., Fang, L., and Jiang, T. (2023). Energy-Efficient ReS(2)-Based Optoelectronic Synapse for 3D Object Reconstruction and Recognition. ACS Appl. Mater. Inter. *15*, 58631–58642. https://doi.org/10.1021/acsami.3c14958.

19. Jung, I., Xiao, J., Malyarchuk, V., Lu, C., Li, M., Liu, Z., Yoon, J., Huang, Y., and Rogers, J.A. (2011). Dynamically tunable hemispherical electronic eye camera system with adjustable zoom capability. Proc. Natl. Acad. Sci. USA *108*, 1788–1793. https://doi.org/10.1073/pnas.1015440108.

20. Qian, H., Wei, D., and Wang, Z. (2023). Bionic iontronics based on nanoconfined structures. Nano Res. *16*, 11718–11730. https://doi.org/10.1007/s12274-023-5705-z.

21. Burgoyne, R.D. (2007). Neuronal calcium sensor proteins: generating diversity in neuronal Ca2+ signalling. Nat. Rev. Neurosci. *8*, 182–193. https://doi.org/10.1038/nrn2093.

22. James, P., Inui, M., Tada, M., Chiesi, M., and Carafoli, E. (1989). Nature and site of phospholamban regulation of the Ca2+ pump of sarcoplasmic reticulum. Nature *342*, 90–92. https://doi.org/10.1038/342090a0.

23. Mitchell, P. (1961). Coupling of phosphorylation to electron and hydrogen transfer by a chemi-osmotic type of mechanism. Nature *191*, 144–148. https://doi.org/10.1038/191144a0.

24. Abe, K., Irie, K., Nakanishi, H., Suzuki, H., and Fujiyoshi, Y. (2018). Crystal structures of the gastric proton pump. Nature *556*, 214–218. https://doi.org/10.1038/s41586-018-0003-8.

25. Li, X., Li, S., Guo, X., Shao, J., Wang, Z.L., and Wei, D. (2023). Triboiontronics for efficient energy and information flow. Matter *6*, 3912–3926. https://doi.org/10.1016/j.matt.2023.08.022.

26. Peng, P., Qian, H., Liu, J., Wang, Z., and Wei, D. (2024). Bioinspired ionic control for energy and information flow. International Journal of Smart and Nano Materials *15*, 198–221. https://doi.org/10.1080/19475411.2024.2305393.

27. Park, S.-J., Gazzola, M., Park, K.S., Park, S., Di Santo, V., Blevins, E.L., Lind, J.U., Campbell, P.H., Dauth, S., Capulli, A.K., et al. (2016). Phototactic guidance of a tissue-engineered soft-robotic ray. Science (New York, N.Y.) *353*, 158–162. https://doi.org/10.1126/science.aaf4292.

28. Zhang, J., Liu, W., Dai, J., and Xiao, K. (2022). Nanoionics from Biological to Artificial Systems: An Alternative Beyond Nanoelectronics. Adv. Sci. *9*, e2200534. https://doi.org/10.1002/advs.202200534.

29. Peng, P., Yang, F., Li, X., Li, S., Wang, Z., and Wei, D. (2024). High-power iontronics enabled by nanoconfined ion dynamics. Cell Reports Physical Science *5*, 101824. https://doi.org/10.1016/j.xcrp.2024.101824.

30. Peng, P., Yang, F., Wang, Z., and Wei, D. (2023). Integratable Paper-Based Iontronic Power Source for All-In-One Disposable Electronics. Adv. Energy Mater. *13*, 2302360. https://doi.org/10.1002/aenm.202302360.

31. Yang, F., Peng, P., Yan, Z.-Y., Fan, H., Li, X., Li, S., Liu, H., Ren, T.-L., Zhou, Y., Wang, Z.L., and Wei, D. (2024). Vertical iontronic energy storage based on osmotic effects and electrode redox reactions. Nat. Energy *9*, 263–271. https://doi.org/10.1038/s41560-023-01431-4.

32. Xiao, K., Chen, L., Chen, R., Heil, T., Lemus, S.D.C., Fan, F., Wen, L., Jiang, L., and Antonietti, M. (2019). Artificial light-driven ion pump for photoelectric energy conversion. Nat. Commun. *10*, 74. https://doi.org/10.1038/s41467-018-08029-5.

33. White, W., Sanborn, C.D., Fabian, D.M., and Ardo, S. (2018). Conversion of Visible Light into Ionic Power Using Photoacid-Dye-Sensitized Bipolar Ion-Exchange Membranes. Joule *2*, 94–109. https://doi.org/10.1016/j.joule.2017.10.015.

34. Xie, X., Crespo, G.A., Mistlberger, G., and Bakker, E. (2014). Photocurrent generation based on a light-driven proton pump in an artificial liquid membrane. Nat. Chem. *6*, 202–207. https://doi.org/10.1038/nchem.1858.

35. Nassi, J.J., and Callaway, E.M. (2009). Parallel processing strategies of the primate visual system. Nat. Rev. Neurosci. *10*, 360–372. https://doi.org/10.1038/nrn2619.

36. Ellis, E.M., Paniagua, A.E., Scalabrino, M.L., Thapa, M., Rathinavelu, J., Jiao, Y., Williams, D.S., Field, G.D., Fain, G.L., and Sampath, A.P. (2023). Cones and cone pathways remain functional in advanced retinal

degeneration. Curr. Biol. *33*, 1513–1522 e4. https://doi.org/10.1016/j.cub.2023.03.007.

37. Wang, X., Chen, C., Zhu, L., Shi, K., Peng, B., Zhu, Y., Mao, H., Long, H., Ke, S., Fu, C., et al. (2023). Vertically integrated spiking cone photoreceptor arrays for color perception. Nat. Commun. *14*, 3444. https://doi.org/10.1038/s41467-023-39143-8.
38. Kandel, Eric R., James H. Schwartz, and Thomas M. Jessell. 2013. Principles of Neural Science. 5th edition. (McGraw-Hill).
39. Zhang, Q., Liu, Z., Wang, K., and Zhai, J. (2015). Organic/Inorganic Hybrid Nanochannels Based on Polypyrrole-Embedded Alumina Nanopore Arrays: pH- and Light-Modulated Ion Transport. Adv. Funct. Mater. *25*, 2091–2098. https://doi.org/10.1002/adfm.201404160.
40. Cheng, Q., Fan, W., He, Y., Ma, P., Vanka, S., Fan, S., Mi, Z., and Wang, D. (2017). Photorechargeable High Voltage Redox Battery Enabled by Ta(3)N(5) and GaN/Si Dual-Photoelectrode. Adv. Mater. *29*, 1700312. https://doi.org/10.1002/adma.201700312.
41. Delgado Andrés, R., Wessling, R., Büttner, J., Pap, L., Fischer, A., Esser, B., and Würfel, U. (2023). Organic photo-battery with high operating voltage using a multi-junction organic solar cell and an organic redox-polymer-based battery. Energy Environ. Sci. *16*, 5255–5264. https://doi.org/10.1039/d3ee01822a.
42. Liu, R., Takakuwa, M., Li, A., Inoue, D., Hashizume, D., Yu, K., Umezu, S., Fukuda, K., and Someya, T. (2020). An Efficient Ultra-Flexible Photo-to-Charging System Integrating Organic Photovoltaics and Supercapacitors. Adv. Energy Mater. *10*, 2000523. https://doi.org/10.1002/aenm.202000523.
43. Gurung, A., Chen, K., Khan, R., Abdulkarim, S.S., Varnekar, G., Pathak, R., Naderi, R., and Qiao, Q. (2017). Highly Efficient Perovskite Solar Cell Photocharging of Lithium Ion Battery Using DC–DC Booster. Adv. Energy Mater. *7*, 1602105. https://doi.org/10.1002/aenm.201602105.
44. Steinberg-Yfrach, G., Liddell, P.A., Hung, S.-C., Moore, A.L., Gust, D., and Moore, T.A. (1997). Conversion of light energy to proton potential in liposomes by artificial photosynthetic reaction centres. Nature *385*, 239–241. https://doi.org/10.1038/385239a0.
45. Zhu, Y., Zhu, R., Yan, L., Fu, H., Xi, Y., Zhou, H., Zhu, G., Zhu, J., and He, H. (2018). Visible-light Ag/AgBr/ferrihydrite catalyst with enhanced heterogeneous photo-Fenton reactivity via electron transfer from Ag/AgBr to ferrihydrite. Appl. Catal., B *239*, 280–289. https://doi.org/10.1016/j.apcatb.2018.08.025.
46. Wang, X., Sun, Y., Wang, G., Li, J., Li, X., and Zhang, K. (2021). TADF-Type Organic Afterglow. Angew. Chem. Int. Ed. *60*, 17138–17147. https://doi.org/10.1002/anie.202105628.
47. Tang, C., Bai, H., Liu, L., Zan, X., Gao, P., Sun, D.D., and Yan, W. (2016). A green approach assembled multifunctional Ag/AgBr/TNF membrane for clean water production & disinfection of bacteria through utilizing visible light. Appl. Catal., B *196*, 57–67. https://doi.org/10.1016/j.apcatb.2016.05.023.
48. Sivula, K., and van de Krol, R. (2016). Semiconducting materials for photoelectrochemical energy conversion. Nat. Rev. Mater. *1*, 15010. https://doi.org/10.1038/natrevmats.2015.10.
49. Patnaik, S., Sahoo, D.P., and Parida, K. (2018). An overview on Ag modified g-C3N4 based nanostructured materials for energy and environmental applications. Renew. Sustain. Energy Rev. *82*, 1297–1312. https://doi.org/10.1016/j.rser.2017.09.026.
50. Wang, C., Chen, X., Wang, L., Makihata, M., Liu, H.-C., Zhou, T., and Zhao, X. (2022). Bioadhesive ultrasound for long-term continuous imaging of diverse organs. Science (New York, N.Y.) *377*, 517–523. https://doi.org/10.1126/science.abo2542.
51. Mildenhall, B., Srinivasan, P.P., Tancik, M., Barron, J.T., Ramamoorthi, R., and Ng, R.N.R.F. (2020). Representing Scenes as Neural Radiance Fields for View Synthesis[A].
52. Yi, L., Hou, B., Zhao, H., and Liu, X. (2023). X-ray-to-visible light-field detection through pixelated colour conversion. Nature *618*, 281–286. https://doi.org/10.1038/s41586-023-05978-w.